Advanced Functional Materials, DOI: 10.1002/adfm.202423055, online on 03 April 2025, 2423055, Vol. 35, No. 36, Sep. 2025

Enhanced pyroelectric response in quenched BNT-based lead-free ferroelectrics for uncooled infrared detection

Meng Shen,[1] Xian zhang,[1] Fangjie Cen,[3] Qingfeng Zhang,[1,5*] Haibo Zhang,[4] Guangzu Zhang,[3] Shenglin Jiang,[4] Yong Chen,[1*] Yongming Hu,[1*] Kui Yao[2*]

[1]Hubei Key Laboratory of Micro-Nanoelectronic Materials and Devices, Key Laboratory of Intelligent Sensing System and Security of Ministry of Education, and School of Microelectronics, Hubei University, Wuhan 430062, China.

[2]Institute of Materials Research and Engineering (IMRE), A*STAR (Agency for Science, Technology, and Research), Singapore 138634, Singapore.

[3]School of Integrated Circuits, Engineering Research Center for Functional Ceramics MOE and Wuhan National Laboratory for Optoelectronics, Huazhong University of Science and Technology, Wuhan 430074, China

[4]School of Materials Science and Engineering, State Key Laboratory of Material Processing and Die & Mould Technology, Huazhong University of Science and Technology, Wuhan, 430074, China

[5]Ministry of Education Key Laboratory of Green Preparation and Application for Functional Materials, Hubei Key Laboratory of Micro-Nanoelectronic Materials and Devices, Hubei Key Laboratory of Polymer Materials, School of Materials Science & Engineering, Hubei University, Wuhan 430062, China.

Email: zhangqingfeng@ hubu.edu.cn; chenyong@hubu.edu.cn; huym@hubu.edu.cn; k-yao@imre.a-star.edu.sg

Keywords: Oxygen vacancies engineering, pyroelectric infrared detector, BNT-based, quenched

Abstract

Excellent pyroelectric performance in environmentally friendly lead-free ferroelectrics is highly demanded for uncooled infrared detector. However, the trade-off between room

temperature pyroelectric coefficient (p_{room}) and depolarization temperature (T_d) remains a major challenge of lead-free ferroelectrics for their device applications. Herein, a superior p_{room} of 13.8×10^{-4} C m^{-2} K^{-1} with high T_d of 155 °C is achieved in quenched BNT-Fe/Mn-NBT sample. Oxygen vacancy engineering is proposed to solve the constraint between p_{room} and T_d in BNT-based ceramics. The local A/B site displacement and oxygen vacancies are constructed in the BNT-Fe/Mn-NBT perovskite structure by quenching treatment, resulting in larger lattice distortion and superior p_{room}. Meanwhile, defect-induced inhomogeneous random field compensates the ferroelectric depolarization field and down-shifts the free energy well, maintaining high T_d. The resulting pyroelectric infrared detector made from the high-performance quenched BNT-Fe/Mn-NBT generates the voltage responsivity of 5906 V W^{-1} and specific detection rate of 1.8×10^{8} cm Hz$^{1/2}$ W^{-1}, which is comparable to the commercial RD-624 type PZT-based pyroelectric infrared detector.

1. Introduction

The pyroelectric devices, which enable the interconversion between heat and electricity, have various applications such as thermal imaging, flame and fire detection, energy harvesting and smart home.[1-4] Lead zirconate titanate (PZT) pyroelectric materials, possessing high pyroelectric coefficient ($p_{room}\geq10\times10^{-4}$ C m^{-2} K^{-1}) and high depolarization temperature (T_d, $T_d\geq150$ °C), dominate the pyroelectric infrared detection applications.[5-7] However, the toxic lead composition poses as serious environmental hazard, contradictory to sustainable development. Tremendous research efforts on the next generation of lead-free ferroelectric materials over past decades have been made to replace PZT materials.[8-12] Among these materials, lead-free $Bi_{0.5}Na_{0.5}TiO_3$ (BNT)-based ceramics have obtained an ambient-temperature p of 2.50×10^{-4} C m^{-2} K^{-1} and even ultrahigh p_{room} exceeding 10×10^{-4} C m^{-2} K^{-1} at the expense of lower T_d below 100 °C.[13] The trade-off between superior p_{room} and high T_d remains a major challenge of BNT-based ferroelectric ceramics for practical pyroelectric applications.

Constructing morphotropic phase boundaries (MPBs) by tuning the chemical composition to form polar nanoscale structures and chemical heterogeneity is an effective approach to optimize pyroelectric property in BNT-based ferroelectric ceramics.[14-16] For instance, engineering

complex stoichiometry in BNT with doping other composition such as $BaTiO_3$ (BT),[14] $(Bi_{0.5}K_{0.5})TiO_3$ (BKT),[17] and $BaTi_{1-x}Zr_xO_3$ (BZT)[13] to form multiple competing polar structure with similar energies, enhances the room temperature p of 27.2×10^{-4} C m^{-2} K^{-1}. However, the formation of polar nanoscale structures breaks long-range translational symmetry of lattice structure and flattens the Gibbs free energy surface, resulting in the reduction of T_d to room temperature. To increase the depolarization temperature, semiconducting ZnO particles are introduced into BNT-BT ceramic to provide charges to compensate the ferroelectric depolarization field.[18] Besides, thermally stabilized $BiAlO_3$ or $Na_{0.5}Bi_{4.5}Ti_4O_{15}$ is solidly dissolved into BNT ceramics to control the heat-induced impurities/defects/ions movement.[19, 20] These approaches strengthen the covalent bond between A/B site atoms and O atoms and even deepen free energy barrier to enhance T_d to ~190 °C, while suppressing pyroelectric coefficients below 10×10^{-4} C m^{-2} K^{-1}. Thus the obtained material cannot meet the requirement of practical applications. Therefore, to overcome the contradiction between high p_{room} and high T_d, a strategy of constructing heterogeneous structure to improve polarization while maintaining deep free energy barrier is demanded.

Defect design in BNT-based ferroelectric ceramics has emerged as an effective strategy for engineering structural and polarization inhomogeneity. [21-23] In this work, we propose the oxygen vacancy engineering to solve the contradictory relationship between high p_{room} and high T_d in BNT-based ceramics. A superior p_{room} of 13.8×10^{-4} C m^{-2} K^{-1} at high T_d of 155 °C is achieved by quenching process without requiring chemical doping in BNT-Fe/Mn-NBT sample. Our systematic study on the performance evolution with the quenching process, atomic-resolved structures with local polarization including defect type and lattice distortion, reveals the mechanism underlying the superior pyroelectric performance. The quenching treatment results in the local A/B site displacement and oxygen vacancy, leading to larger lattice distortion and superior room temperature p. Meanwhile, the inhomogeneous random field induced by defect compensates the ferroelectric depolarization field and down-shifts the free energy well, thus maintaining high T_d. The trade-off between superior room temperature p and high T_d can be achieved accordingly. Therefore, the voltage responsivity of 5906 V W^{-1}, noise equivalent power of 2.0×10^{-9} W Hz$^{-1/2}$ and specific detection rate of 1.8×10^{8} cm Hz$^{1/2}$ W^{-1} have been

obtained using the quenched BNT-Fe/Mn pyroelectric infrared detector, which is comparable to the commercial RD-624 type PZT-based pyroelectric infrared detector.

2. Results and Discussion

2.1 Microstructures and atomic-resolved structures with local polarization

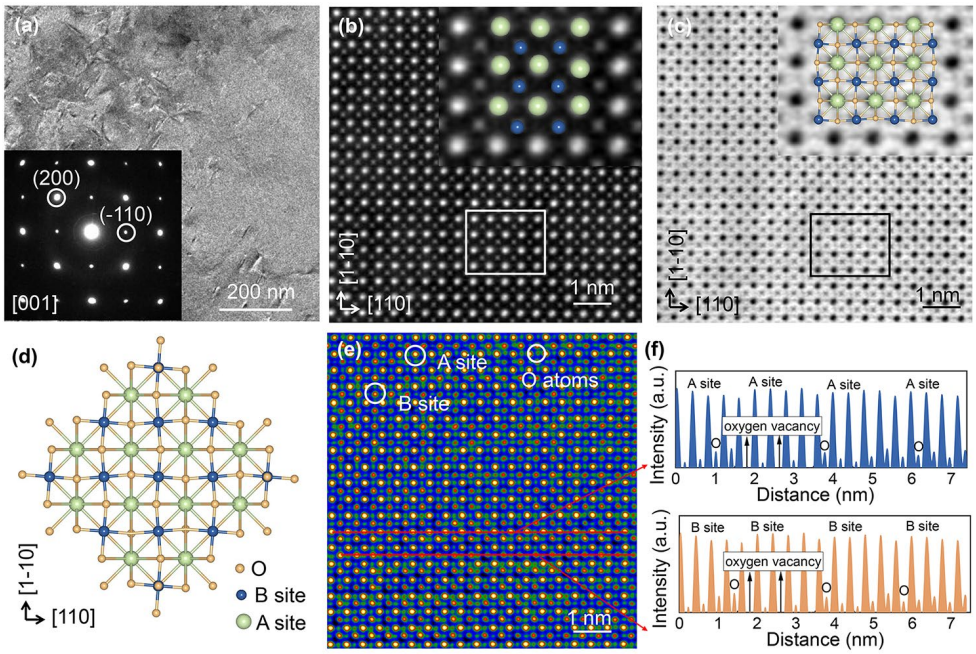

Figure 1. (a) The low-magnitude HRTEM image of quenched BNT-Fe/Mn-NBT sample and the corresponding SAED patterns along [001]. The atomic-resolution (b) HAADF-STEM and (c) ABF-STEM images of quenched BNT-Fe/Mn-NBT sample along [001] and the partially enlarged view of the area labeled in square. (d) The lattice structural characteristics of quenched BNT-Fe/Mn-NBT sample along [001]. (e) The integrated differential phase contrast (iPDC) STEM image of quenched BNT-Fe/Mn-NBT sample along [001] and (f) the intensity profile of A/B site and O atoms highlighted in red line on Figure 1(e).

To reveal the microstructure of the BNT-Fe/Mn-NBT samples, the surface scanning electron microscopic (SEM) images and the X-ray diffraction (XRD) are conducted with results as presented in Figure S1 and Figure S2. It is observed from Figure S1 that the grain size of quenched sample is more uniform and refined, in the range of 1.5-4.5 μm. XRD Rietveld refinements (Figure S2) and Lattice parameters of BNT-Fe/Mn-NBT samples (Table S1) show that the main crystalline phase of both samples is tetragonal perovskite structure,[24, 25] and quenched BNT-Fe/Mn-NBT sample possesses enlarged lattice parameters (a=b=5.498 Å,

c=3.888 Å) compared to unquenched BNT-Fe/Mn-NBT sample (a=b=5.488 Å, c=3.878 Å). High resolution transmission electron microscopy (HRTEM) and selected-area electron diffraction (SAED) for BNT-Fe/Mn-NBT samples further confirm the conclusion of XRD Rietveld refinement. According to the results of SAED along [001] zone axis and lattice fringes as presented in Figure S3 and Figure 1a, both samples exhibit a high crystalline quality with tetragonal perovskite structure.

To further explore the local atomic configuration in quenched BNT-Fe/Mn-NBT sample, atomic-resolution high-angle annular dark-field (HAADF), annular bright-field (ABF) and the integrated differential phase contrast (iPDC) scanning transmission electron microscopy (STEM) are conducted along [001] zone axis, as shown in Figure 1b-f. The energy dispersive spectrum (EDS) and the corresponding two-dimensional element mapping of quenched BNT-Fe/Mn-NBT sample are displayed in Figure S4 and Figure S5. It can be seen that A site columns (Bi/Na) show higher contrast while B site columns (Ti/Fe/Mn) and O columns are less noticeable in HAADF and ABF images.[26, 27] Local parts of HAADF-STEM image (marked in square) are further enlarged and A/B site atoms are labeled as shown in the inset of Figure 1b. Similarly, A/B site atoms and O atoms are marked in the magnified ABF-STEM image (Figure. 1c) to provide the information of O atoms. The crystalline structure along [001] zone axis is presented in Figure 1d and colorized iPDC-STEM images are presented in Figure 1e-f to reveal the variation of atomic structure. As shown in Figure 1e-f, clearly resolved A site atom columns and slightly visible B site atom columns are alternately arranged and A/B site atom columns present subtle shifts. Moreover, as shown in Figure 1e-f, besides A/B site atoms, O atom columns are clearly visible in the iPDC-STEM image, and they are unevenly distributed and even deficient in some sites.

The origins of the oxygen vacancies can be due to the Fe/Mn acceptor doping and/or volatilization of bismuth/sodium oxide at high temperature. When the sample is slowly cooled down (unquenching process), oxygen vacancies of the sample are re-oxidized according to equation ($V_O^{\cdot\cdot} + \frac{1}{2}O_2 \rightarrow V_O^{\times} + 2h^{\cdot}$), leading to low concentration of oxygen vacancies in unquenched BNT-Fe/Mn-NBT sample. For quenched BNT-Fe/Mn-NBT sample, the oxygen vacancies formed at high temperature have no time to be re-oxidised and remain in the sample,

resulting in high oxygen vacancy concentrations.

The relative displacements of B-site ions to the center of its four adjacent A site ions are quantitatively calculated by using 2D Gaussian peak fitting as shown in Figure 2a. The corresponding polarization magnitude and polarization angle mappings are presented in Figure 2b-c. The local polarization vectors show an obvious disordered state in some areas, illustrating the existence of inhomogeneous random field. In addition, deviation of A-A site column distance and B-B site column distance from the average lattice parameters are observed as shown in Figure 2d-f, suggesting that the enhanced local lattice distortion caused by quenching process. Figure S6 reveal the XRD patterns of the BNT-NBT and BNT-Fe/Mn-NBT samples with both quenched and unquenched processing. It can be observed from Figure S3(b) that both quenched BNT-NBT and BNT-Fe/Mn-NBT samples have faint splitting peaks at 47°. These effects are attributed to higher rhombohedral distortion, which is consistent with the phase field simulation as shown in Figure 7. In contrast, both unquenched BNT-NBT and BNT-Fe/Mn-NBT sample do not show rhombohedral distortion. Therefore, the superior pyroelectric performance of quenched BNT-Fe/Mn-NBT sample can be attributed to the enhanced local lattice distortion and oxygen vacancies caused by quenching process.

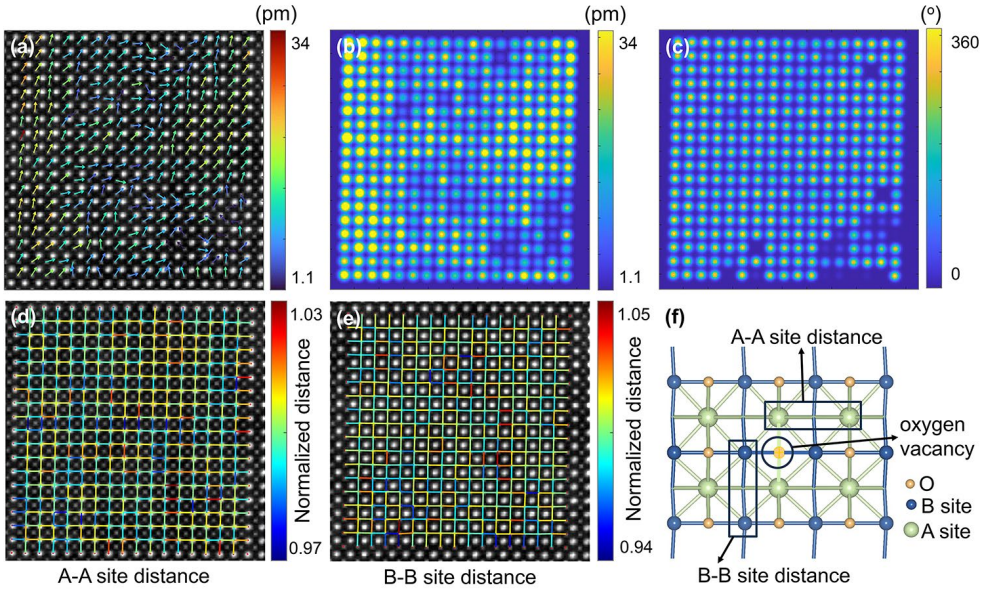

Figure 2. (a) The Atomically resolved HAADF-STEM image with polarization vector mapping. (b) The polarization magnitude mapping, and (c) the polarization angle mapping along [001]. The statistical mapping of (d) A-A site ion distance and (e) B-B site ion distance for the region

in (a) and (f) the corresponding structural mode.

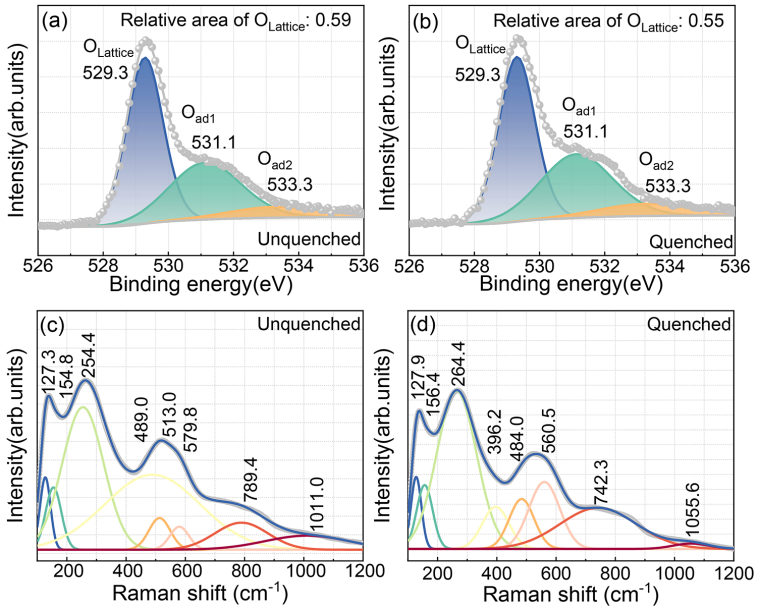

Figure 3. The O 1s XPS spectra of (a) unquenched and (b) quenched BNT-Fe/Mn-NBT samples. The Raman spectra of (c) unquenched and (d) quenched BNT-Fe/Mn-NBT samples.

2.2 Defect engineering and lattice distortion

To investigate the effect of quenching process on oxygen vacancy concentration and chemical state of the BNT-Fe/Mn-NBT samples, X-ray photoelectron spectra (XPS) of both quenched and unquenched samples are measured and the spectra of Bi 4f, Na 1s, Ti 2p and O 1s are presented in Figure S7a-c and Figure 3a-b. As shown in Figure S7a-b, for both unquenched and quenched samples, Bi 4f doublet peaks located at 158.7 eV and 164.0 eV and the Na 1s peak appeared at the binding energy of 1071.2 eV is assigned to Na^{+} and Bi^{3+} oxidation state, respectively. As shown in Figure S7c, the Ti 2p spectra of both samples comprise of four Gaussian peaks. Besides the overlapping Bi $4d_{3/2}$ peaks around 465.3 eV, doublet Gaussian peaks located at 457.8 eV and 463.4 eV for Ti $2p_{3/2}$ and Ti $2p_{1/2}$ are observed, attributed to Ti^{4+} oxidation state. [28] As shown in Figure 3a-b, the O 1s spectra of both quenched and unquenched samples are fitted with three Gaussian peaks located at 529.3 eV, 531.1 eV and 533.3 eV. The first O 1s peak originates from the lattice oxygen, the second and third peaks may correspond to adsorbed oxygen.[29-31] The relative areas of lattice oxygen for unquenched and quenched samples are 0.59 and 0.55, respectively, indicating the reduction of lattice oxygen with quenching process. This implies the higher oxygen vacancy concentration in quenched

BNT-Fe/Mn-NBT samples. The increasing concentration of oxygen vacancy facilitates local lattice distortion and multiple orientation directions, which is consistent with the STEM results.

To further confirm the lattice distortion of quenched BNT-Fe/Mn-NBT samples, the Raman spectra of BNT-Fe/Mn-NBT samples are presented in Figure 3c-d. As shown in Figure. 3c-d, all the Raman spectra show eight Raman vibration modes, which are divided into three regions including low wavenumbers (≤200 cm^{-1}), middle wavenumbers (200~400 cm^{-1}) and high wavenumbers (≥400 cm^{-1}).[32, 33] The spectral range below 200 cm^{-1} is derived from A-O stretching vibrations and the two lower wavenumber modes of A-O vibrations show barely change with quenching process. The Raman bands between 200~400 cm^{-1} originate from B-O vibrations involving Ti, Fe, and Mn cations in BNT-Fe/Mn-NBT samples. A shift to higher wavenumbers of the Raman peak from 254.4 cm^{-1} to 264.4 cm^{-1} with increasing intensity is observed for quenched samples, which suggests a strengthening of B-O vibrations after quenching. The bands above 400 cm^{-1} wavenumbers are related with vibrations of TiO_6 octahedral. The Raman peak located at 579.8 cm^{-1} is associated with the stretching modes of the TiO_6 octahedral. With quenching processing, the spectra exhibit a decreasing wavenumber from 579.8 cm^{-1} to 560.5 cm^{-1}, revealing that the high level of structural disorder strongly affects the dynamic of the TiO_6 octahedra.[34]

2.3 Electrical properties and their depolarization temperature

Figure 4a shows the temperature dependent relative dielectric constant (ε_r) and loss (tanδ) for both unquenched and quenched BNT-Fe/Mn-NBT samples. As shown in Figure 4a, the ε_r and tanδ from room temperature to 150 °C slightly decrease after quenching process, indicating the enhancement of pyroelectric figure of merits (FOMs) (as shown in Figure 5) due to the inversely proportional relationship between FOMs and ε_r. In addition, there are two dielectric peaks for both samples, [35, 36] one is the ferroelectric to paraelectric phase transition (T_m) at ~ 350 °C, and the other is the non-ergodic to ergodic relaxor state (T_d) near 150 °C, which corresponds to the peak pyroelectric temperature as shown in Figure 5a. As shown in Figure 4a, the T_m remains unaltered while the T_d increases from 135 °C to 155 °C with quenching process, suggesting an increase in temperature stability. The electrical impedance properties including the Z'-Z'' spectra and frequency-dependent Z'' spectra of both unquenched and quenched BNT-Fe/Mn-

NBT samples are shown as Figure S8. It can be seen from Figure S8 that the electrical resistivity of BNT-Fe/Mn-NBT samples decreases after quenching process, which suggests the electronic conductivity of BNT-Fe/Mn-NBT sample increases. The conductivity of quenched BNT-Fe/Mn-NBT sample remains in a relatively small range although the conductivity of the quenched sample increases. Appropriately increasing the conductivity of the material is beneficial to improve pyroelectric properties of the material. This is because the pyroelectric coefficient is described as the change in the spontaneous polarization vector with temperature according to the following equation: $p = \frac{dP}{dT}$. The appropriate amount of electrons is conducive to the absorption of heat, which leads to the quick change of temperature and makes the material have good pyroelectric properties.

The temperature dependent piezoelectric coefficient (d_{33}) for BNT-Fe/Mn-NBT samples further verifies the improved temperature stability. As shown in Figure 4b, the plots of d_{33} versus temperature reveal that the quenched sample show an enhanced thermal depolarization temperature (T_d) compared to the unquenched sample. Moreover, with the temperature increasing from 25 ºC to T_d, the d_{33} for quenched sample enhances from 79 to 102 while that of the unquenched sample improves from 102 to 156, indicating a superior polarization characteristics and thermal stability. The reason is probably that the improved concentration of oxygen vacancy and Ti^{3+} facilitates local lattice distortion. Figure 4c illustrates the room temperature polarization-electric field (*P*-*E*) hysteresis loops for BNT-Fe/Mn-NBT samples. Both quenched and unquenched samples present typical ferroelectric hysteresis loops. The remanent polarization (P_r) and the saturated polarization (P_s) of quenched BNT-Fe/Mn-NBT sample increases to 47.2 μC cm^{-2} and 57.7 μC cm^{-2}, respectively, which is consistent with the polarization characteristics as measured in Figure 4b.

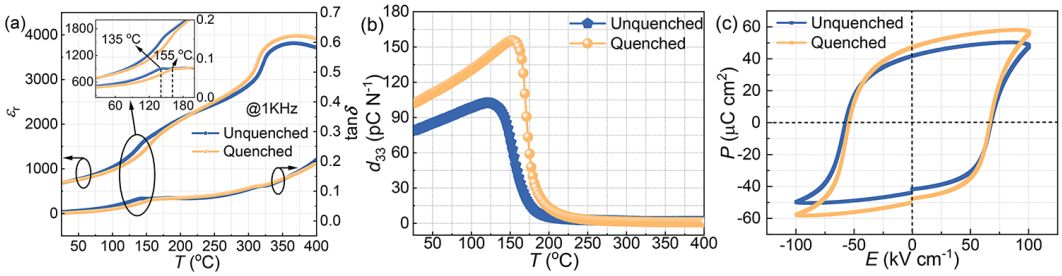

Figure 4. (a) The temperature dependence of dielectric constant (ε_r) and loss (tanδ), (b) the

temperature dependence of d_{33} , and (c) the *P-E* loops for both unquenched and quenched BNT-Fe/Mn-NBT samples.

2.4 Superior pyroelectric response and infrared detector

Figure 5a presents the temperature dependent pyroelectric coefficient (p) curves for both unquenched and quenched BNT-Fe/Mn-NBT samples. As shown in Figure 5a, both the peak pyroelectric temperature (T_d) and room temperature pyroelectric coefficient (p) of quenched samples are enhanced by engineering local oxygen vacancies and multiple orientation directions, which exhibits a superior overall pyroelectric performance with a high T_d of 155 ºC and a large room pyroelectric coefficient of 13.8×10^{-4} C m^{-2} K^{-1} for quenched BNT-Fe/Mn-NBT samples. With the pyroelectric properties of BNT-NBT and BNT-Fe/Mn-NBT samples shown in Figure S9, it can be seen that the pyroelectric coefficient of BNT-Fe/Mn-NBT samples has a slight increase near room temperature while the depolarization temperature is greatly reduced after doping Fe/Mn. While with quenching process, both near room-temperature pyroelectric coefficient and depolarization temperature are enhanced as shown in Figure 5(a). Therefore, superior pyroelectric performance of quenched BNT-Fe/Mn-NBT sample is mainly caused by the quenching process instead of Fe or Mn acceptor doping.

The figure of merits (FOMs) of F_d, F_v, and F_i for both unquenched and quenched pyroelectric samples are evaluated based on the following equations: [1, 3, 37]

$$F_d = p/\left(C_v\sqrt{(\varepsilon_0\varepsilon_r tan\theta)}\right) \quad (1)$$

$$F_v = p/(C_v\varepsilon_r\varepsilon_0) \quad (2)$$

$$F_i = p/C_v \quad (3)$$

where C_v is the volume specific heat (2.89 J cm^{-3} K^{-1}) of the samples and ε_0 is the permittivity of free space (8.854×10^{-12} F m^{-1}). [38, 39] As shown in Figure 5b-d, the FOMs (F_d, F_v, and F_i) shows the similar trend with the near room-temperature pyroelectric coefficients for BNT-Fe/Mn-NBT samples. The quenched pyroelectric ceramics possess enhanced F_d, F_v and F_i of 34.3 μPa^{-1}, 0.04 m^2 K^{-1}, and 5.0 mV^{-1} compared with that of unquenched ceramics. The comprehensive pyroelectric performance of both unquenched and quenched BNT-Fe/Mn-NBT

samples is shown in Figure 5e. The room-temperature p, T_d, and FOMs of quenched BNT-Fe/Mn-NBT samples improve significantly in comparison with the unquenched pyroelectric ceramics. The comparison of pyroelectric performance of quenched BNT-Fe/Mn-NBT samples with that of typical lead-based and lead-free pyroelectric ceramics are provided in Figure 5f. As shown in Figure 5f the room-temperature p or T_d of quenched BNT-Fe/Mn-NBT samples surpass the state-of-the-art lead-free pyroelectric materials and comparable to the lead-based pyroelectric ceramics,[3, 20, 37, 40-48] showing great application potential for pyroelectric infrared detection.

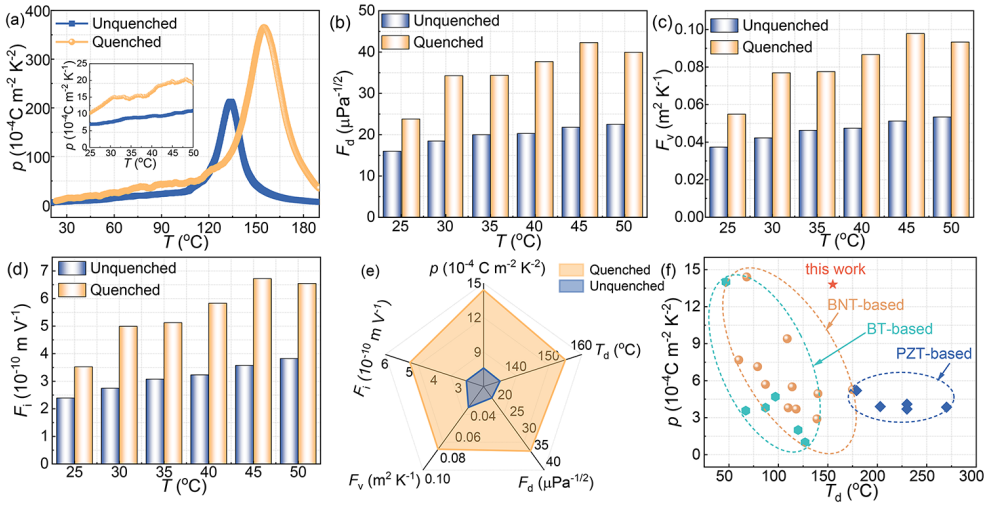

Figure. 5 (a) The temperature-dependent pyroelectric coefficient for both unquenched and quenched BNT-Fe/Mn-NBT samples. The figure of merits (FOMs) (b), F_d, (c) F_v, (d) F_i for BNT-Fe/Mn-NBT samples. (e) The comparison of comprehensive pyroelectric performance for both unquenched and quenched BNT-Fe/Mn-NBT samples. (f) The comparison of pyroelectric performance of quenched BNT-Fe/Mn-NBT samples with that of typical lead-based and lead-free pyroelectric ceramics.

Owing to the outstanding comprehensive pyroelectric performance of quenched BNT-Fe/Mn-NBT samples, pyroelectric infrared detector is fabricated from quenched BNT-Fe/Mn-NBT. The equivalent circuit diagram and the product photo are shown Figure 6a-b. The pyroelectric infrared detector consists of a Fresnel lens, a pyroelectric sensing element, a gate resistance (R_g) and a junction field-effect transistor (JFET). The pyroelectric charge generated by the sensing element is converted into a voltage signal through the gate resistance (R_g), and

the junction field-effect transistor (JFET) generates a conduction channel to output a stable voltage according to the value of pyroelectric signal. It can be seen from Figure 6c that the output pyroelectric voltage signal of the pyroelectric infrared detector made from quenched BNT-Fe/Mn-NBT is stable and the peak-peak voltage (U_p) value is ~2.64 V. Meanwhile, as shown in Figure 6d, the peak noise voltage (U_n) of pyroelectric infrared detector made from quenched BNT-Fe/Mn-NBT is less than 50 mV. The voltage responsivity (R_V), noise equivalent power (*NEP*) and specific detection rate (D^*) are essential parameters for evaluating the overall performance of pyroelectric infrared detector by following formulas: [48]

$$R_V = \frac{U}{W} = \frac{U_p}{PA_s} \tag{4}$$

$$NEP = \frac{P}{U_p/U_n} \tag{5}$$

$$D^* = \frac{U_p/U_n}{P}\sqrt{A\Delta f} \tag{6}$$

where P, A_s, A, and Δf are the input radiation power of 1.06×10^{-7} W, the amplification factor of 72.5 dB, the area of pyroelectric sensing element of 0.05 cm^2, and working bandwidth of 2.7 Hz, respectively. According to the formulas, the R_V, *NEP* and D^* of the pyroelectric infrared detector are 5906 V W^{-1}, 2.0×10^{-9} W $Hz^{-1/2}$, and 1.8×10^{8} cm $Hz^{1/2}$ W^{-1}, respectively. The output performance of quenched BNT-Fe/Mn-NBT derived pyroelectric infrared detector reaches that of the commercial lead-based pyroelectric infrared detector.

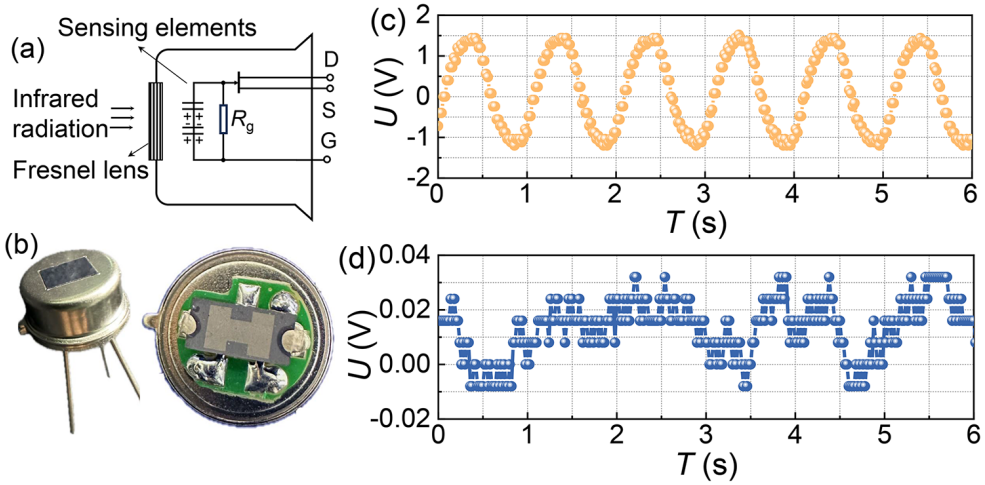

Figure 6. (a) The circuit for voltage mode of the pyroelectric infrared detector. (b) A photo of the pyroelectric infrared detector made from quenched BNT-Fe/Mn-NBT ceramic. (c) The

output pyroelectric voltage signal and (d) the noise voltage signal for pyroelectric infrared detector with quenched BNT-Fe/Mn-NBT.

2.5 Relationship between macroscale properties and the microstructures

To shed light on the relationship between high pyroelectric performance and the microstructures, phase field simulation (Supplementary Section I) is carried out to study the contributions from oxygen vacancies and local lattice distortion by quenching. The 3D ferroelectric domain structures of BNT-Fe/Mn-NBT samples with unquenched and quenched process are simulated as shown in Figure 7a-d. As shown in Figure 7a-b, the 3D structures of both unquenched and quenched samples display a nonuniform feature with the polarizations in the matrix tending to tetragonal-like symmetry, while the defect regions maintain obvious different polarization directions tending to point along the out-of-plane direction, which is similar with rhombohedral-like symmetry.[22] This is mainly because the inhomogeneous random field derived from oxygen vacancies and B site ion displacements that breaks the polarization continuity. The existence of oxygen vacancy and B site ion displacements are critical to forming rhombohedral-like domain structures, which isolates the defect regions from the matrix. The isolated rhombohedral-like domains distribute more widely with quenching process and have a higher energy state as shown in Figure 7c. They are more susceptible to the temperature change to transform into tetragonal-like domain structures with a lower energy, which facilitate the polarization rotation between the rhombohedral-like domain and the tetragonal-like matrix accompanied by the transformation. Therefore, a high room temperature pyroelectric response can be achieved. With increasing temperature, the rhombohedral-like domains gradually transform into tetragonal-like symmetry and the overall structures approach a homogeneous distribution as shown in Figure 7c-d. Accordingly, the energy well of quenched BNT-Fe/Mn-NBT sample tends to be separated by higher energy barrier as shown in Figure 7f, which means the domain switching requires more heat, corresponding to the larger T_d.

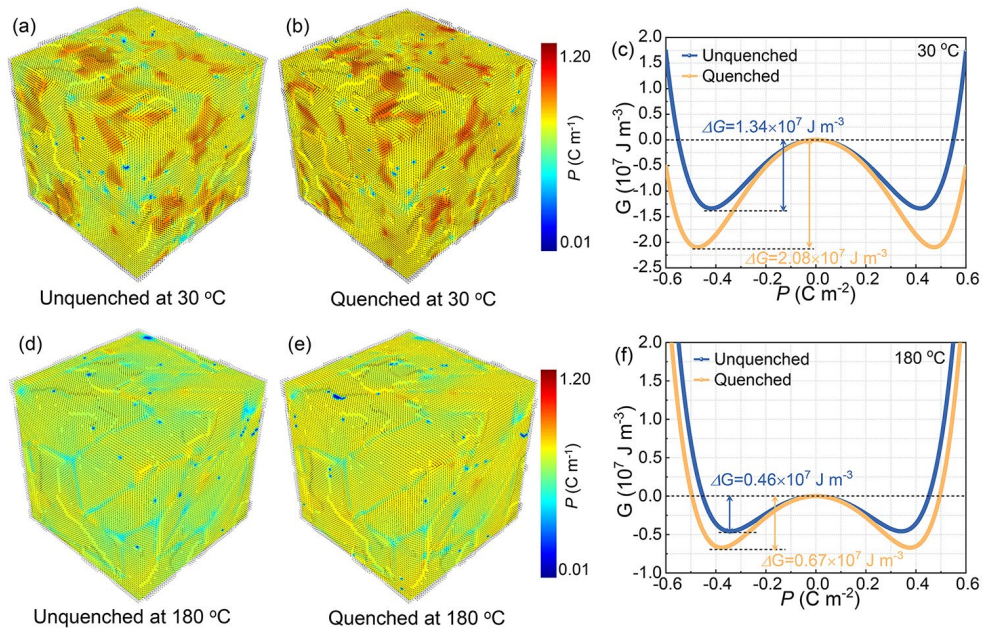

Figure 7. The 3D ferroelectric domain structures of BNT-Fe/Mn-NBT samples with (a) unquenched and (b) quenched, at 30 °C, and (c) the corresponding Gibbus free energy profiles. The 3D ferroelectric domain structures of BNT-Fe/Mn-NBT samples with (d) unquenched and (e) quenched, at 180 °C, and the corresponding Gibbus free energy profiles.

3. Conclusion

In summary, a large p_{room} of 13.8×10^{-4} C m^{-2} K^{-1} at high T_d of 155 °C has been achieved by quenching process without requiring chemical doping in BNT-Fe/Mn-NBT sample. Oxygen vacancy engineering is proposed as a strategic solution to improve both p_{room} and T_d by breaking their contradictory constraint in BNT-based ceramics. A systematic study on atomic-resolved structures with local polarization has been conducted, including defect type and lattice distortion, electrical properties and their depolarization temperature, for revealing the mechanism underlying the superior pyroelectric performance. The quenching treatment results in the local A/B site displacement and oxygen vacancy, leading to larger lattice distortion and the superior p_{room}. Meanwhile, the inhomogeneous random field induced by defect compensates the ferroelectric depolarization field and down-shifts the free energy well, thus maintaining high T_d and achieving the trade-off between large p_{room} and high T_d. As a result, the pyroelectric infrared detector made from the quenched BNT-Fe/Mn-NBT generates the voltage responsivity of 5906 V W^{-1}, noise equivalent power of 2.0×10^{-9} W Hz$^{-1/2}$ and specific detection rate of

1.8×10^{8} cm $Hz^{1/2}$ W^{-1}, which is comparable to the commercial RD-624 type PZT-based pyroelectric infrared detector. The theoretical understanding provides a strategic guidance to design high-performance pyroelectric infrared detector.

4. Experimental Methods

4.1 Preparation of ceramic samples and detector

Solid-state reaction method was used to prepare both unquenched and quenched $0.997Bi_{0.5}Na_{0.5}TiO_3$-$0.003Na_{0.5}Bi_{4.5}Ti_4O_{15}$ (BNT-NBT) and $0.997Bi_{0.5}Na_{0.5}Ti_{0.995}(Fe_{0.25}Mn_{0.75})_{0.005}O_3$-$0.003Na_{0.5}Bi_{4.5}Ti_4O_{15}$ (BNT-Fe/Mn-NBT) ferroelectric ceramic samples. According to the chemical formula, reagent grade metal oxide Bi_2O_3 (99%, Sinopharm), Na_2CO_3 (99.8%, Sinopharm), TiO_2 (98%, Sinopharm), Fe_2O_3 (99.5%, Sinopharm), $MnCO_3$ (99.95%, Sinopharm) were ball milled in ethanol with zirconia for 12~18 h. After drying and calcination at 800~900 °C for 2 h, the mixtures were ball milled for 12~18 h again, then dried and granulated with 5% polyvinyl alcohol. After the mixed powders were pressed into a disk in a abrasive tool at 5~10 MPa, sintering was carried out in aluminum oxide crucibles at 1130~1160 °C for 2 h with increasing temperature rate of 3 °C min^{-1}. For unquenched samples, the sample was cooled to room temperature in the furnace, and for quenched samples, the sample was taken out of furnace at 1130~1160 °C for rapid cooling in air.

4.2 Characterization of atomic-resolved structures and defect type

SEM (Zeiss Geminisem 300) and XRD (D8 Advance, Bruker, Germany) were employed to analyze the microstructures of the samples. The refined data were obtained through Rietveld method based on the slow-scan XRD data by using the GSAS-EXPGUI software and the $Na_{0.5}Bi_{0.5}TiO_3$ (space group P4bm) CIF was chosen as the initial model.[49, 50] The high-resolution electron microscopy (HRTEM) and selected area electron diffraction (SAED) images were obtained by the field emission transmission electron microscope (FETEM) (Tecnai G2 F30, Netherlands). The atomic-resolution high-angle annular dark-field (HAADF), annular bright-field (ABF), the integrated differential phase contrast (iPDC) images and the energy dispersive spectrum (EDS) were measured by scanning transmission electron microscopy

(STEM) (FEI Spectra 300). 2D Gaussian fitting was used to obtain the position information of all atom columns, and a prewritten script on MATLAB was employed to calculate the A-A site distance, B-B site distance and the polarization vector mapping.[27, 51] The X-ray photoelectron spectroscopy (XPS) was conducted with photoelectron spectrometer (Thermo scientific ESCAlab 250xi, Thermo, America) and the Raman scattering spectra of the samples were measured with laser Raman spectrometer (LabRAM HR Evolution, Horiba, Japan).

4.3 Measurement of electrical and pyroelectric properties

To study the electrical properties, the samples were ground into 0.3 mm in thickness and coated with silver paste on both sides with the electrode diameter of 6 mm and then fired at 600 °C for 15 min. After that, all the samples were poled in silicone oil using a high-voltage power supply (ET2673D-10kV) with applied field of 5 kV mm^{-1} for 20 min at room temperature. The relative dielectric constant and loss were measured with a Dielectric Properties Testing System (DPTS-RT-1000, Wuhan Yanhe Technology Co. Ltd., China). Polarization-electric field (*P*-*E*) hysteresis loops were measured with Ferroelectric Analyzer System (TF2000, aixACCT, Germany). The pyroelectric properties were measured using Pyroelectric Test System (PCTS-3000, Wuhan Yanhe Technology Co. Ltd., China) for poled samples at a heating rate of 2 °C min^{-1}.

4.4 Fabrication and testing of pyroelectric device

For pyroelectric device fabrication, the samples were firstly poled in silicone oil using a high-voltage power supply (ET2673D-10kV) with applied field of 5 kV mm^{-1} for 20 min at room temperature. After thinned and polished to 80~120 μm by abrasive paper, the samples were cut into rectangle with 2.5 mm×5.0 mm to obtain the pyroelectric sensitive element. After cleaning and drying, Ni-Cd electrodes were sputtered on both sides of quenched BNT-Fe/Mn samples by thermal evaporation coater (FD-3500K, Kyky Technology Development Ltd.), after that the sensitive element was welded on a commercial printed circuit board (PCB) base by spot welding machine (YCD-5100C) and finally was encapsulated in cap with Fresnel lens to obtain the pyroelectric infrared detector. The output voltage signal was measured by pyroelectric infrared tester (IRTS,Wuhan Yanhe Technology Co. Ltd., China) at frequency of 2.7 Hz.

Acknowledgements

This work was supported by the National Natural Science Foundation of China (Grant Nos. U21A20500, 52102128 and 52272107), and the Open Project Fund of State Key Laboratory of Refractories and Metallurgy (Wuhan University of Science and Technology, Grant No. G202207). The author from IMRE acknowledges supports from A*STAR, under RIE2020 AME Programmatic Fund (Grant No. A20G9b0135).

References

[1] C. R. Bowen, J. Taylor, E. LeBoulbar, D. Zabek, A. Chauhan, R. Vaish, *Energy Environ. Sci.* **2014**, 7, 12.

[2] X. Yuan, J. Shi, Y. Kang, J. Dong, Z. Pei, X. Ji, *Adv. Mater.* **2024**, 36, 3.

[3] D. Zhang, H. Wu, C. R. Bowen, Y. Yang, *Small* **2021**, 17, 51.

[4] H. He, X. Lu, E. Hanc, C. Chen, H. Zhang, L. Lu, *J. Mater. Chem. C* **2020**, 8, 5.

[5] R. Mondal, M. A. M. Hasan, J. M. Baik, Y Yang, *Mater. Today* **2023**, 66.

[6] L. Li, X Zhao, X. Li, B. Ren, Q. Xu, Z. Liang, W. Di, L. Yang, H. Luo, X. Shao, J. Fang, N. Neumann, J. Jiao, *Adv. Mater.* **2014**, 26, 16.

[7] L. Bian, X. Qi, K. Li, Y. Yu, L. Liu, Y. Chang, W. Cao, S. Dong, *Adv. Funct. Mater.* **2020**, 30, 25.

[8] K. Song, R. Zhao, Z. L. Wang, Y. Yang, *Adv. Mater.* **2019**, 31, 36.

[9] E. Meirzadeh, D. V. Christensen, E. Makagon, H. Cohen, I. Rosenhek-Goldian, E. H. Morales, A. Bhowmik, J. M. G. Lastra, A. M. Rappe, D. Ehre, M. Lahav, N. Pryds, I. Lubomirsky, *Adv. Mater.* **2019**, 31, 44.

[10] M. Shen, K. Liu, G. Zhang, Q. Li, G. Zhang, Q. Zhang, H. Zhang, S. Jiang, Y. Chen, K. Yao, *Nat. Commun.* **2023**, 14, 1.

[11] A. Kumar, R. Vaish, S. Kumar, V. P. Singh, M. Vaish, V. Singh Chauhan, K. S. Srikanth, *Energy Technol.* **2018**, 6, 5.

[12] Y. Huang, T. Zheng, J. Wu, *Nano Energy* **2024**, 110184.

[13] M. Shen, W. Li, M. Y. Li, H. Liu, J. Xu, S. Qiu, G. Zhang, Z. Lu, H. Li, S. Jiang, *J. Eur. Ceram. Soc.* **2019**, 39, 5.

[14] L. Chen, N. Wang, Z. Zhang, H. Yu, J. Wu, S. Deng, H. Liu, H. Qi, J. Chen, *Adv. Mater.* **2022**, 34, 44.

[15] W. Feng, B. Luo, S. Bian, E. Tian, Z. Zhang, A. Kursumovic, J. L. MacManus-Driscoll, X. Wang, L. Li, *Nat. Commun.* **2022** 13, 1.

[16] W. Li, G. Tang, G. Zhang, H. M. Jafri, J. Zhou, D. Liu, Y. Liu, J. Wang, K. Jin, Y. Hu, H. Gu, Z. Wang, J. Hong, H. Huang, L. Chen, S. Jiang, Q. Wang, *Sci. Adv*. **2021**, 7, 5.

[17] M. Zhou, R. Liang, Z. Zhou, X, Dong, *J. Am. Ceram. Soc.* **2020**, 103, 1.

[18] J. Zhang, Z .Pan, F. F. Guo, W. C. Liu, H. Ning, Y. B. Chen, M. H. Lu, B. Yang, J. Chen, S. T. Zhang, X. Xing, J. Rödel, W. Cao, Y. F. Chen, *Nat. Commun.* **2015**, 6, 1.

[19] J. Jia, S. Guo, S. Yan, F. Cao, C. Yao, X. Dong, G. Wang, *Appl. Phys. Lett.* **2019**, 114, 3.

[20] L. Hu, B. Fan, Z. Fang, G. Zhang, Q. Zhang, G. Zhang, H. Zhang, S. Jiang, Y. Chen, M. Shen, *Acta Mater.* **2022**, 238, 118194.

[21] Y. X. Liu, W. Qu, H. C. Thong, Y. Zhang, Y. Zhang, F. Z. Yao, T. N. Nguyen, J. W. Li, M. H. Zhang, J. F. Li, B. Han, W. Gong, H. Wu, C. Wu, B. Xu, K. Wang, *Adv. Mater.* **2022** 34, 29.

[22] H. Luo, H. Liu, H. Huang, Y. Song, M. G. Tucker, Z. Sun, Y. Yao, B. Gao, Y. Ren, M. Tang, H. Qi, S. Deng, S. Zhang, J. Chen, *Sci. Adv.* **2023**, 9, 5.

[23] L. Lai, B. Li, S. Tian, Z. Zhao, S. Zhang, Y. Dai, *Adv. Mater.* **2023**, 35, 29.

[24] J. Yin, X. Shi, H. Tao, Z. Tan, X. Lv, X. Ding, J. Sun, Y. Zhang, X. Zhang, K. Yao, J. Zhu, H. Huang, H. Wu, S. Zhang, J. Wu, *Nat. Commun*. **2022**, 13, 1.

[25] J Yin, H Zong, H Tao, X Tao, H Wu, Y Zhang, L. D. Zhao, X. Ding, J. Sun, J. Zhu, J. Wu, S. J. Pennycook, *Nat. Commun.* **2021**, 12, 1.

[26] M. Waqar, H. Wu, K. P. Ong, H. Liu, C. Li, P. Yang, W. Zang, W. H. Liew, C. Diao, S. Xi, D. J. Singh, Q. He, K. Yao, S. J. Pennycook, J. Wang, *Nat. Commun.* **2022**, 13, 1.

[27] C. Long, Z. Su, H. Song, A. Xu, L. Liu, Y. Li, K. Zheng, W. Ren, H. Wu, X. Ding, *Energy Storage Mater*. **2024**, 65,103055.

[28] Z. Gao, Z. Jia, K. Wang, X. Liu, L. Bi, G. Wu, Chem. Eng. J. 2020, 402, 125951.

[29] J. Wang, D. N. Mueller, E. J. Crumlin, *J. Eur. Ceram. Soc.* **2024**: 116709.

[30] D. J. Morgan, *Surf. Interface Anal.* **2023**, 55, 845.

[31] H. Idriss, *Surf. Sci.* **2021**, 712, 121894.

[32] T. Li, C. Liu, P. Shi, X. Liu, R. Kang, C. Long, M. Wu, S. Cheng, S. Mi, Y. Xia, L. Li, D. Wang, X. Lou, *Adv. Funct. Mater.* **2022**, 32, 32.

[33] S. Wang, F. Yan, J. Qian, G. Ge, Z. Fu, Z. Pan, F. Zhang, J. Lin, K. Zeng, C. Chen, B. Shen, Z. Liu, J. Zhai, *Energy Storage Mater.* **2024**, 66,103155.

[34] Y. Mendez-González, A. Peláiz-Barranco, A. L. Curcio, A. D. Rodrigues, J. D. S. Guerra, *J. Raman Spectrosc.* **2019**, 50, 7.

[35] D. Li, D. Zhou, D. Wang, W. Zhao, Y. Guo, Z. Shi, T. Zhou, S. K. Sun, C. Singh, S. Trukhanov, A. S. B. Sombra, *Small* **2022**, 19, 2206958.

[36] H. Liu, Q. Q. Zhang, H. Luo, J. Zhu, *Appl. Phys. Lett.* **2022**, 120, 072901.

[37] K. S. Srikanth, V. P. Singh, R. Vaish, *J. Eur. Ceram. Soc.* **2017**, 37, 13.

[38] J. Chen, L. Wu, L. Duan, D. Liu, *Ferroelectrics* **2021**, 585, 1.

[39] M. Shen, Y. Qin, Y. Zhang, M. A. Marwat, C. Zhang, W. Wang, M. Li, H. Zhang, G. Zhang, S. Jiang, *J. Am. Ceram. Soc.* **2019**, 102, 7.

[40] R. W. Whatmore, S. J. Ward, *J. Appl. Phys.* **2023**, 133 .

[41] S. Patel, M. Kumar, AIP Adv. **2020**, 10, 8.

[42] A. Gaur, N. Saurabh, N. Upadhyay, *J. Phys. Chem. Solids* **2024**, 192, 112084.

[43] N. Saurabh, S. Patel, *Mater. Today Commun.* **2024**, 41, 110784.

[44] A. M. Balakt, C. P. Shaw, Q. Zhang. *Ceram. Int.* **2017**, 43, 4.

[45] A. Ray, M. Nayak, H. Joardar, *Chemical Physics Impact*, **2024**, 8, 100555.

[46] N. Saurabh, S. Patel, *J. Mater. Sci. Mater. Electron.* **2024**, 35, 20.

[47] L. Wen, X. Wu, J. Yin, Small **2024**, 2307326.

[48] Z. Wu, M. Zhang, X. Jiang, X. Ke, Y. Cai, L. Cao, J. Li, H. Jia, C. Li, C. M. Leung, F. Wang, *J. Am. Ceram. Soc.* **2023**, 106, 11.

[49] T. Li, X. Jiang, J. Li, A. Xie, J. Fu, R. Zuo, *ACS Appl. Mater. Interfaces* **2022**, 14, 22263.

[50] B. Guo, Y. Yan, M. Tang, Z. Wang, Y. Li, L. Zhang, H. Zhang, L. Jin, G. Liu, *Chem. Eng. J.* **2021**, 420, 130475.

[51] L. Chen, S. Deng, H. Liu, J. Wu, H. Qi, J. Chen, *Nat. Commun.* **2022**, 13, 1.